港湾技術研究所報告

REPORT OF THE PORE AND HARBOUR RESEARCH INSTITUTE

MINISTRY OF TRANSPORT

VOL. 32 NO. 3 Sept. 1993

NAGASE, YOKOSUKA, JAPAN

港湾技術研究所報告（Report of P. H. R. I.）

第32巻　第３号（Vol.32, No.３）1993年９月（Sept. 1993）

目　次（CONTENTS）

REPORT OF PORT AND
HARBOUR RESEARCH INSTITUTE
Vol.32, No. 3 (Sept. 1993)

1. Longshore current distribution on a bar-trough beach — Field measurements at HORF and numerical model —

Yoshiaki KURIYAMA *
Yasushi OZAKI **

Synopsis

Field measurements of longshore current have been carried out at Hazaki Oceanographical Research Facility (HORF) when waves broke over bars. A float was used for the measurements; the measurement method with the float is confirmed to be useful by the calibrations with an electromagnetic current meter. Eighty-five percent of the measured longshore current distributions have peak velocities in the onshore sides of the bar crests.

A numerical model for nearshore current in the surf zone is developed with the consideration of the momentum fluxes due to mass transport under bores, broken waves. This model consists of two models, a wave height transformation model for directional random waves and a nearshore current model. The significant wave heights calculated by the present model agree well with the measured ones. The longshore current velocity distributions over the bars and the troughs calculated by the present model, of which each has a peak velocity in the onshore side of the bar crest, agree with the measured ones, while the distributions calculated by a previous model disagree with the measured ones.

Key Words: Longshore current, Nearshore current, Field measurement, Numerical model, Longshore bar, Bar- trough beach

* Senior Research Engineer, Hydraulic Engineering Division
** Member of Littoral Drift Laboratory, Hydraulic Engineering Division

港湾技術研究所報告
第32巻第3号 (1993. 9)

1．バー型海岸における沿岸流速分布
―波崎海洋研究施設における現地観測と数値モデルの開発―

栗山善昭*・尾崎　靖**

要　旨

バー型海岸における沿岸流速分布の特性を把握するために，1987年から1990年までの4年間，全長427mの波崎海洋研究施設（以下，HORF）に沿って1日1回，岸沖方向に15～30mの間隔で沿岸流速を観測した。観測では直径約20cmのフロートを使用した。本観測方法の有効性は，電磁流速計による検定で確認された。

バーが形成されており，そのバー上で砕波が生じていたときの沿岸流速分布の特性を，バー周辺での最大沿岸流速の発生位置を調べることによって検討した。

続いて，新たな沿岸流速数値モデルを開発した。砕波帯内のボアによる運動量フラックスをモデル化し，従来の海浜流モデルに組み込んだ。海浜流の外力を計算するための浅海域における波浪変形数値モデルも，沿岸流速数値モデルの一部として開発した。

本研究で得られた主要な結論は以下の通りである。

1）バー型海岸において砕波がバー上で生じているときの沿岸流速分布のうち，バーの頂部よりも岸側で最大沿岸流速が生じていたケースは全体の85％で，バーの頂部よりも沖側で最大流速が生じていたケースは全体の15％であった。

2）ボアによる運動量フラックスを考慮した沿岸流速数値モデルでは，沿岸方向に一様な海岸におけるバー頂部よりも岸側で最大値を持つ沿岸流速分布形を再現することができる。ただし，従来のモデルはこの分布形を再現することができない。

　この結果は，ボアによる運動量フラックスが海浜流に対して大きな影響を及ぼすことを示している。

3）浅海域の波浪変形数値モデルによる計算値はHORFでの観測値と良く一致した。

キーワード：沿岸流速，海浜流，現地観測，数値モデル，沿岸砂州，バー型海岸

* 水工部　主任研究官
** 水工部　漂砂研究室

Contents

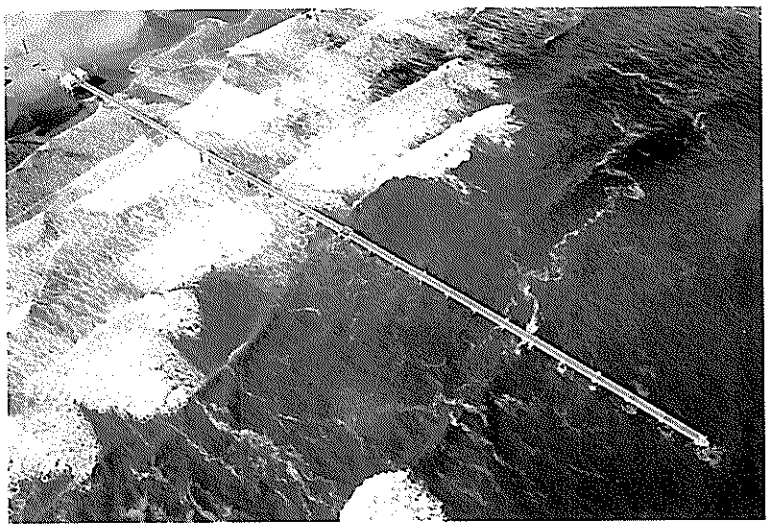

Photograph 1 Aerial view of Hazaki Oceanographical Research Facility (HORF).

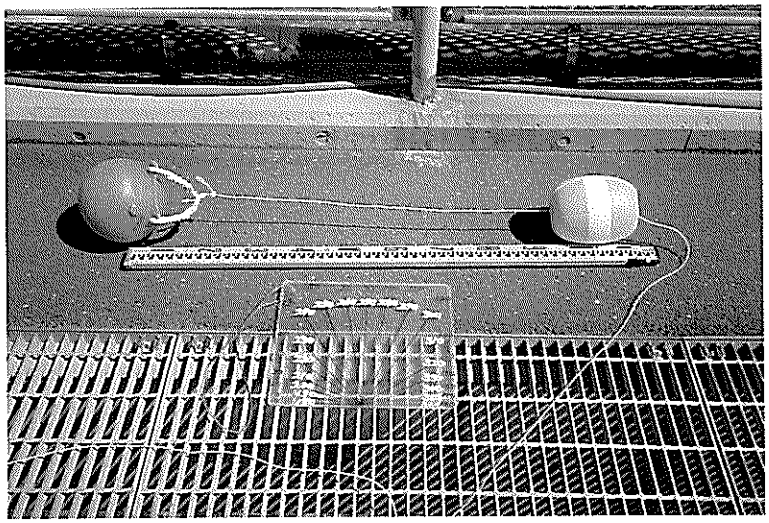

Photograph 2 Spherical float (orange), identification buoy (yellow) and protractor for the measurement of nearshore current.

Photograph 3 Releasing a float.

Photograph 4 Measuring nearshore current velocity.

Photograph 5 Measuring nearshore current velocity.

Photograph 6 Measuring the transport direction of the float.

1. Introduction

In recent years, cross-shore distributions of longshore current on barred beaches have been investigated; barred beaches are observed in the field more frequently, especially after storms, than planar beaches. *Whitford and Thornton* (1988) measured a distribution that has a peak velocity in the offshore side of a bar crest in the field. *Allender and Ditmars* (1981) and *Greenwood and Sherman* (1986) measured not only this type of distribution but also the other type of distribution that has a peak velocity in the onshore side of a bar crest. The latter distribution was also measured by *Church and Thornton* (1992).

Although these two types of the longshore current distribution on a barred beach were shown through the investigations, the frequencies of the two distributions were not discussed owing to the limited data of longshore current distributions on barred beaches. One objective of this paper is to discuss the characteristics of longshore current distributions on barred beaches on the basis of abundant field data. For this purpose, we have carried out field measurements of longshore current distributions on a barred beach during four years by using a pier.

The other objective of this paper is to develop a numerical model for nearshore current in the surf zone that includes the momentum fluxes due to mass transport under bores, broken waves. In the one-dimensional models for longshore current proposed by *Ebersole and Dalrymple* (1980), and *Larson and Kraus* (1991), the driving force of the longshore current is the cross-shore gradient of the radiation stress. This gradient is largest in the offshore side of a bar crest owing to the large dissipation of wave energy due to wave breaking. Thus the longshore current distribution derived by them is the former one, which has a peak velocity in the offshore side of a bar crest. The latter distribution, which has a peak velocity in the onshore side of a bar crest, is not generated by their one-dimensional models.

Symonds and Huntley (*komer*,1983) and *Allender and Ditmars* (1981) suspected that the longshore gradient of wave setup causes the latter distribution. We, however, sometimes observed the latter distribution from a pier when no rip currents were observed around the pier; no rip currents probably indicate that the longshore gradient of the wave setup is very small. These observations suggest another generation mechanism of the latter distribution. Therefore we pay attention to the development and decay of bores over a bar and a trough as a generation mechanism of the latter distribution, and develop a numerical model for nearshore current that includes the momentum fluxes due to mass transport under bores, which are not included in a previous model for nearshore current. The longshore current velocities calculated by the present model are compared with the measured ones and the values calculated by a previous model.

2. Outline of field measurements

2.1 Measurement site and method

Field measurements have been carried out during four years commencing on January 5, 1987, at the Hazaki Oceanographical Research Facility (HORF). The HORF is the pier of 427m long and 6.9m above the low water level, which faces to the Pacific Ocean as shown in **Figure 1. Photograph 1** shows an aerial view of the HORF.

Figure 2 shows the side view of the HORF and the mean profile during the four years. Short vertical lines on the beach profile indicate the standard deviations of the beach profile changes. The horizontal axis expresses the offshore distance. The cross-shore location is defined according to this coordinate; for example, the expression of "P145m" indicates the location where the offshore distance

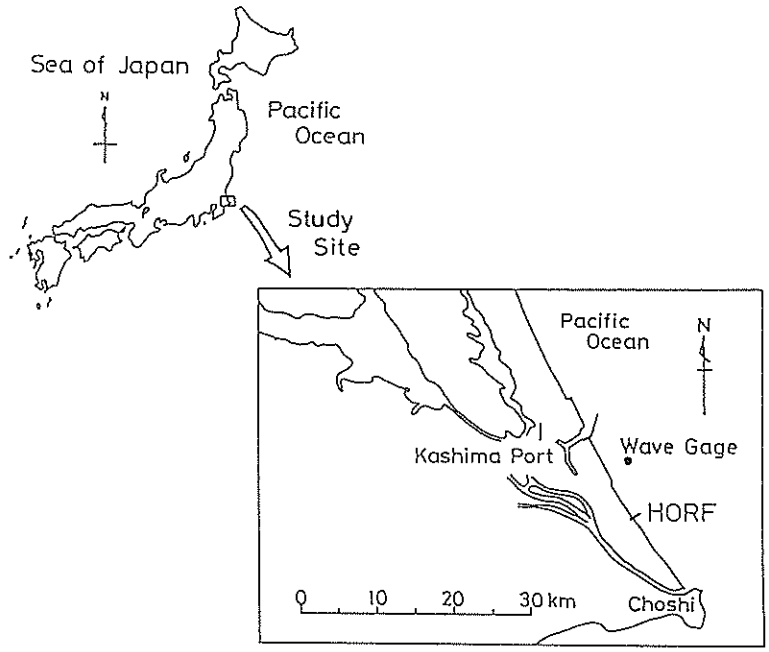

Figure 1 Study site.

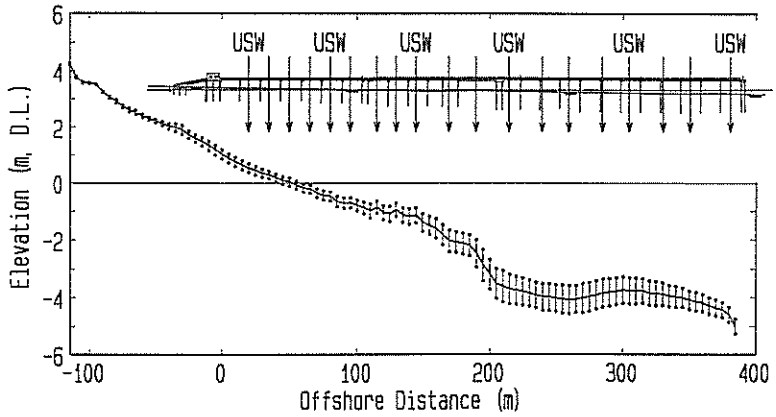

Figure 2 Side view of the HORF, mean profile during the four years and measurement points.

is equal to 145m. The mean beach slope along the HORF is about 1/60. A trough is frequently formed in the area between P190m and P220m, and a bar crest is often located near P300m. The arrows indicate the measurement points of longshore current, and those with "USW" also indicate the locations of ultrasonic wave gages.

A spherical float having a diameter of 0.2m as shown in **Figure 3**, which is the orange one in **Photograph 2**, was used in the measurements. We measured nearshore current velocities at 1m below the water surface to avoid the effects of winds and waves. Thus the density of the float was adjusted to

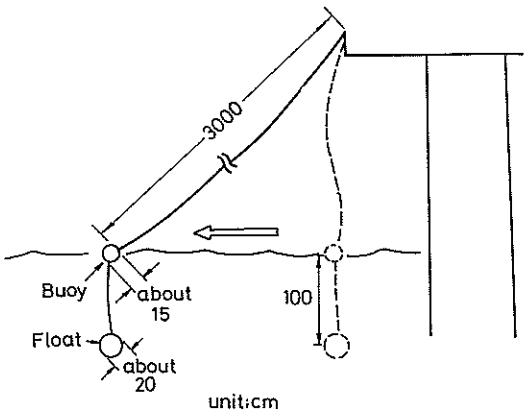

Figure 3 Float for measurements.

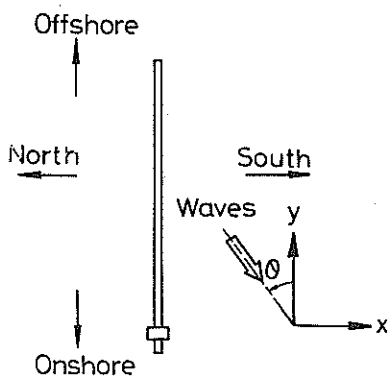

Figure 4 Definition sketch of co-ordinate system.

be a little larger than that of sea water. The float was connected with an identification buoy by 1m long rope as shown in **Figure 3** and in **Photograph 2.** The length of the rope was adequately shortened when mean water depth is small.

In the measurements, the float attached to a 30m line was released from the HORF as shown in **Photograph 3,** and the time for full extension of the line was measured with a stopwatch as shown in **Photographs 4** and **5.** The current velocity was calculated with the time and the length of the line. The transport direction of the float due to nearshore current was observed with a protractor as shown in **Photograph 6.** At each point, nearshore currents were measured three times.

It takes about 90 minutes to measure the nearshore currents along the HORF. The mean breaking positions and the breaking wave directions were observed visually.

The beach profiles from P0m to the tip of the HORF were measured every 5m with a 5kg lead weight, and those in the onshore side of P0m were measured with a level and a staff. Water surface elevations at seven points were measured for twenty minutes every hour at a sampling frequency of 2Hz with the ultrasonic wave gages; the location are shown in **Figure2.**

Figure 4 shows the co-ordinate system used in this paper. The positive directions of x-axis and y-axis are southward and seaward, respectively. The vertical axis extends upwards. Elevations are relative to the datum level in Hasaki. The wave direction is defined relative to the shoreward direction and positive in counterclockwise.

2.2 Calibration of the measurement method

Longshore current velocities measured with the float are compared with those measured with an electromagnetic current meter to check the accuracy of the measurement method with the float. The electromagnetic current meter was installed in the sea at P145m by using a ladder as shown in **Figure 5.** When the distance between the sensor of the current meter and the mean water level was about 1m, longshore current velocities were measured with the float and with the current meter simultaneously.

Figure 6 shows the relationship between the longshore components of the nearshore current velocities measured with the float, U_{FLOAT}, and those measured with the current meter, U_{EMC}; triangles show the data obtained when the longshore components of the wind velocities were over +8m/s. Although the velocities measured with the float are larger than those measured with the current meter, there is very strong correlation between them. Furthermore, the effects of winds to the measured

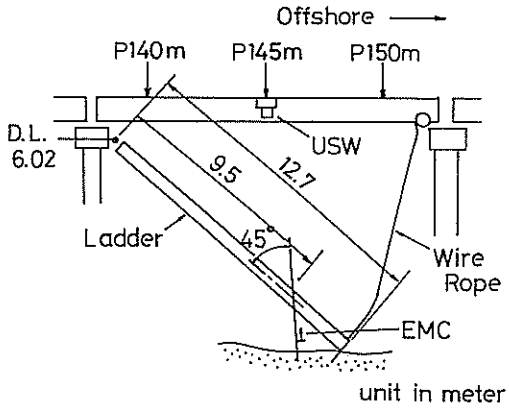

Figure 5 Install of electromagnetic current meter at P145m.

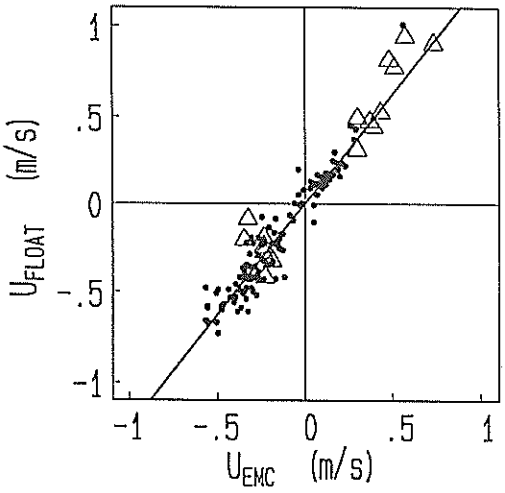

Figure 6 Relationship between U_{EMC} and U_{FLOAT}.

velocities with the float were small. Through this calibration, this simple method with the float was confirmed to be useful for the measurement of longshore current velocity. Even though the field measurement with this method is simple, easy and reliable, it is very hard on a cold and rainy day in winter.

The relationship between U_{EMC} and U_{FLOAT} is expressed as

$$U_{EMC} = 0.81\ U_{FLOAT}. \qquad (1)$$

In the following analysis, the values of U_{EMC} are used.

We suppose that the reason why the velocities measured with the float are larger than those measured with the current meter is the effect of waves to the identification buoy. The identification buoy is easily transported in the direction of wave propagation by waves because the buoy is on the water surface, where the mass flux due to waves is concentrated. The float is consequently transported in the same direction. The longshore direction of the wave propagation usually agrees with the direction of the longshore current. Thus the velocities measured with the float are larger than those measured with the current meter.

3. Location of a peak velocity of the longshore current over a bar and a trough

We investigate the longshore current distributions measured when bars and troughs were formed and waves broke over the bars. When a wave height or an incident wave angle is small, the nearshore current is usually small and is easily affected by the longshore topographic inhomogeneities. Thus the data of which peak longshore current velocities over bars and troughs are below 0.25m/s are eliminated. Consequently fifty-two longshore current distributions are selected for the following analysis.

The frequency distributions of significant wave height, H_0, significant wave period, T_0, wave steepness, H_0/L_0, and absolute value of incident wave angle, θ_{tip}, at the fifty-two measurements are shown in **Figures 7(1) to 7(4)**, respectively. The values of H_0 and T_0 are those at the water depth of 23.4m, and are calculated from the field data obtained with the ultrasonic wave gage at the water depth

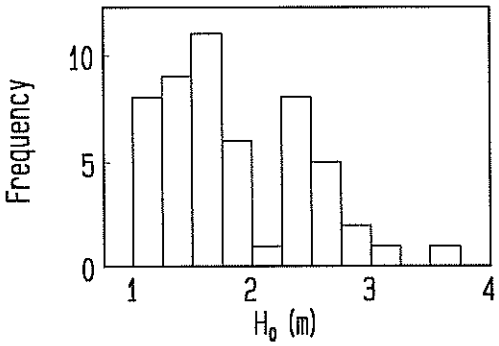

Figure 7(1) Frequency distribution of H_0.

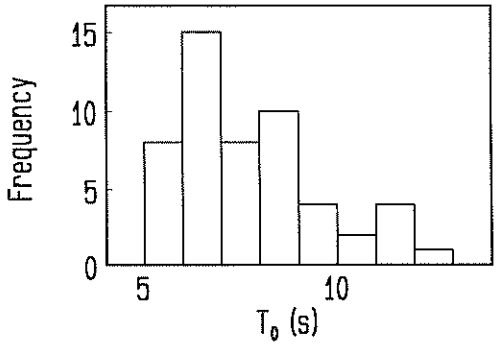

Figure 7(2) Frequency distribution of T_0.

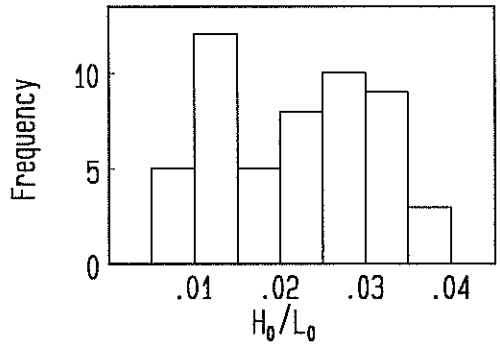

Figure 7(3) Frequency distribution of H_0/L_0.

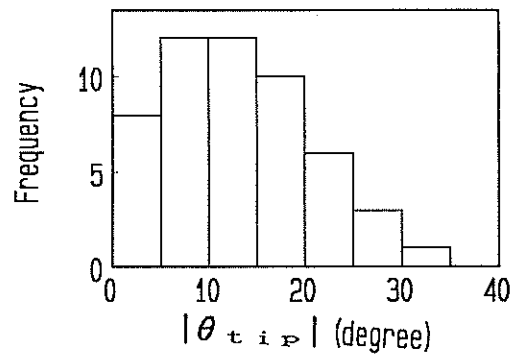

Figure 7(4) Frequency distribution of the absolute value of θ_{tip}.

of 23.4m; the location of the gage is shown in **Figure 1**. The value of H_0/L_0 is calculated with the values of H_0 and T_0. The value of θ_{tip} is that measured visually at the tip of the HORF. The ranges of H_0 and T_0 are from 1m to 3.6m, and from 5s to 13s; the mean values of H_0 and T_0 are 1.9m and 7.7s. Accordingly the range and the mean value of H_0/L_0 are from 0.007 to 0.04, and 0.022. The absolute value of θ_{tip} varies from 0° to 30°. We consider that an incident wave angle visually observed has an error of about ±5°. Thus a longshore current velocity over 0.25m/s was measured even though θ_{tip} was equal to zero; the real incident wave angle is not supposed to have been zero.

Figures 8(1) and **8(2)** show the relationships between the offshore distance of the bar crest, y_{bar}, and that of the trough, y_{trough}, and between the water depth at the bar crest, h_{bar}, and that at the trough, h_{trough}, with their frequency distributions. The bar crests are formed around P290m, while the troughs are formed around P220m. The values of h_{bar} and h_{trough} range from 2.4m to 4.5m, and from 3.7m to 6.0m, respectively; the mean values of h_{bar} and h_{trough} are 3.4m and 4.7m.

The relationship between the peak longshore current velocity in the area from the tip of the HORF to the trough, U_{peak}, and the mean longshore current velocity in the area, U_{ave}, is shown in **Figure 9** with their frequency distributions. The differences between U_{peak} and U_{ave} are mainly from 0.05m/s to 0.25m/s. While the values of U_{peak} are widely distributed from 0.25m/s to 1.1m/s, most of the values are below 0.6m/s.

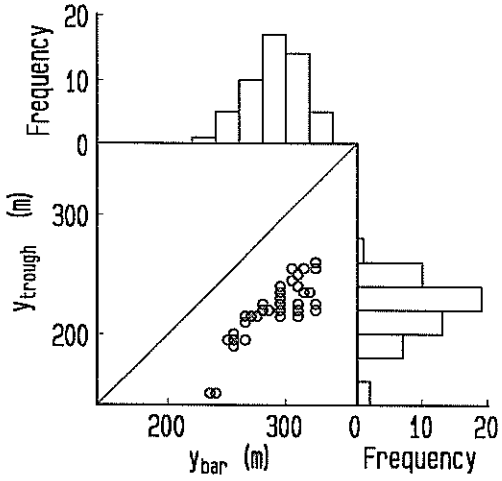

Figure 8(1) Relationship between y_{bar} and y_{trough}, and their distributions.

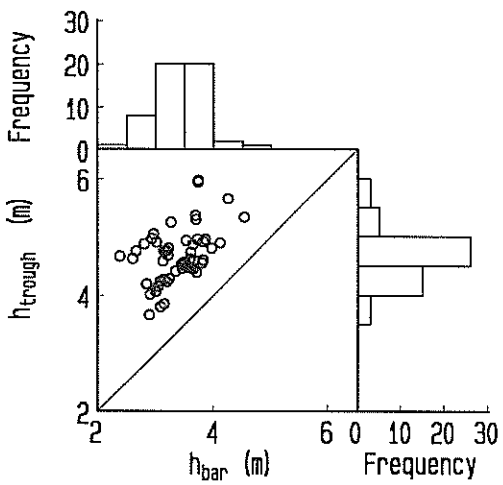

Figure 8(2) Relationship between h_{bar} and h_{trough}, and their distributions.

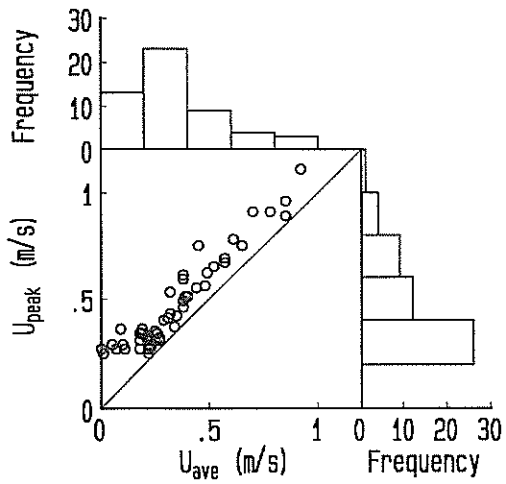

Figure 9. Relationship between U_{ave} and U_{peak}, and their distributions.

The fifty-two distributions measured at the HORF are classified into two groups from the view point of the location of a peak velocity of the longshore current over a bar and a trough. A distribution in one group has a peak velocity in the onshore side of a bar crest, and that in the other group has a peak velocity in the offshore side of a bar crest.

Three examples of the longshore current distributions are shown. Two examples belong to the former group, and one example belongs to the latter one. **Figure 10(1)** shows a distribution that has a peak velocity in the onshore side of a bar crest; the signs of the longshore current velocities are changed from minus to plus in this figure. This distribution was measured on March 28, 1989. Horizontal arrows indicate the breaker zones. A vertical arrow indicates the location of the peak

velocity over the bar and the trough. Waves broke over the bar, reformed over the trough and broke again around P145m. The longshore current velocity increases onshoreward in the offshore side of the bar crest. After reaching maximum slightly onshoreward of the bar crest, the longshore current velocity decreases onshoreward. The velocity increases again in the secondary surf zone.

Another example of the distribution that has a peak velocity in the onshore side of a bar crest is shown in **Figure 10(2)**. This distribution was measured on November 28, 1987. Waves broke not only in the offshore side of the bar crest but also in the onshore side. After reforming over the trough, waves broke again between P140m and P80m. The longshore current velocity increases slightly in the onshore side of the bar crest, and reaches maximum at the trough. From P220m to P190m, the velocity decreases, and increases again in the secondary breaker zone between P140m and P80m.

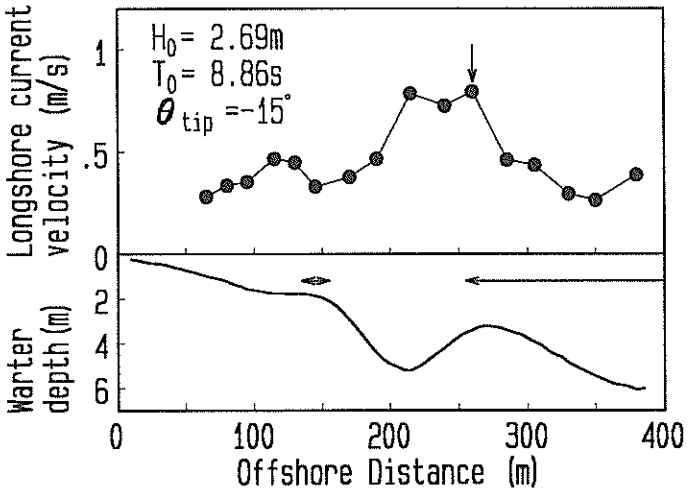

Figure 10(1) Longshore current distribution and beach profile on March 28, 1989.

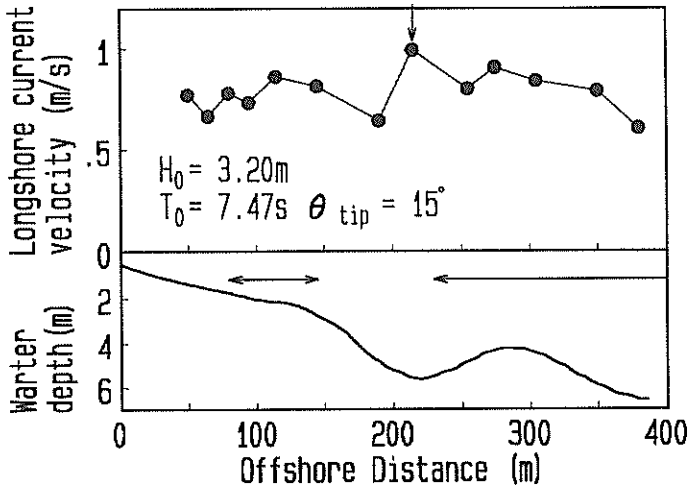

Figure 10(2) Longshore current distribution and beach profile on November 28, 1987.

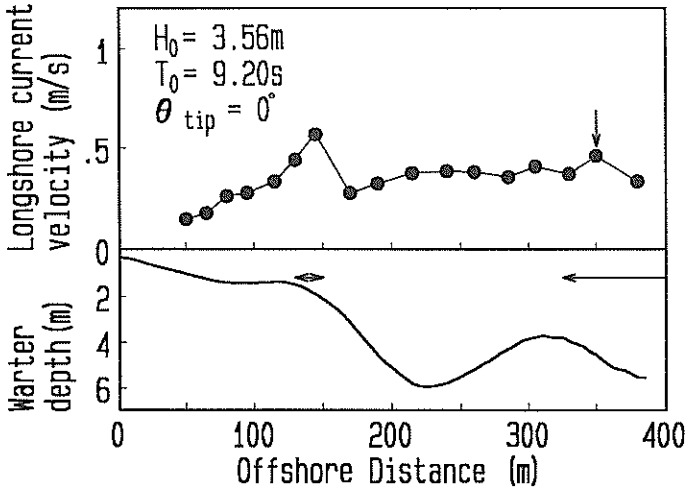

Figure 10(3) Longshore current distribution and beach profile on May 12, 1989.

Figure 10(3) shows the example of the longshore current distribution that has a peak velocity in the offshore side of a bar crest. The distribution was measured on May 12, 1989. After breaking over the bar, waves reformed over the trough and broke again around P140m. The longshore current velocity increases from P380m to P350m. After reaching peak at P350m, the longshore current velocity gradually decreases onshoreward over the bar and the trough. The velocity increases again in the secondary breaker zone.

The relationship between y_{bar} and the offshore distance of the location of the peak longshore velocity over the bar and the trough, y_{peak} is shown in **Figure 11(1)** with their frequency distributions. While the values of y_{bar} are concentrated in the area from P280m to P320m, the values of y_{peak} are

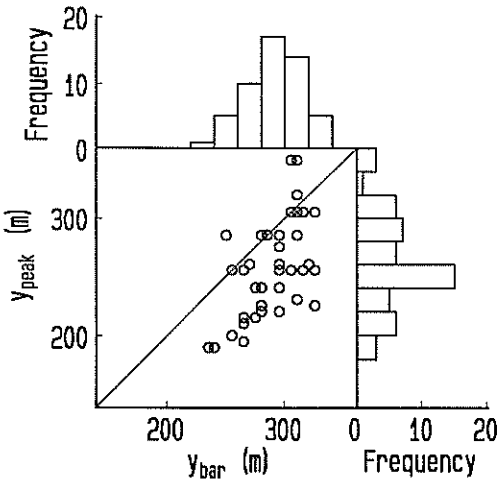

Figure 11(1) Relationship between y_{bar} and y_{peak}, and their distributions.

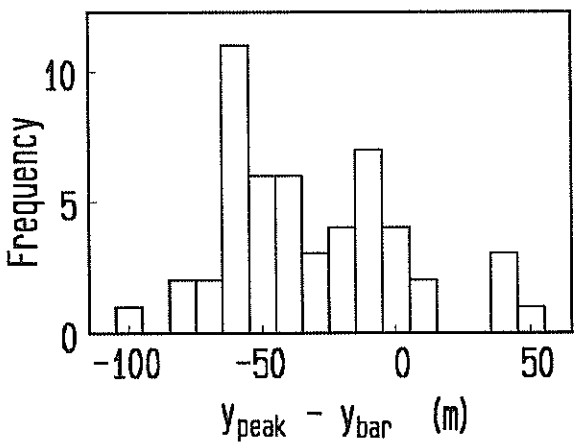

Figure 11(2) Frequency distribution of the offshoreward distance from y_{bar} to y_{peak}.

widely distributed from P180m to P340m.

Figure 11(2) shows the frequency distribution of the offshoreward distance from y_{bar} to y_{peak}. When the value of y_{bar} - y_{peak} is plus, the peak velocity is located in the offshore side of a bar crest. Although each of the longshore current distributions calculated by the one-dimensional models has a peak velocity in the offshore side of the bar crest (*Ebersole and Dalrymple*, 1980; *Symonds and Huntley*, (*komar*,1983); *Larson and Kraus*, 1991), 85 percent of the distributions measured at the HORF have peak velocities in the onshore sides of the bar crests.

We consider that momentum fluxes due to mass transport under bores are significant for a longshore current distribution in the surf zone; the fluxes are not considered in the one-dimensional models for longshore current and in a previous model for nearshore current. In the next chapter, a new model that contains the momentum fluxes due to mass transport under bores is developed.

4. Model for nearshore current in the surf zone

The new model consists of two computational distinct numerical models, a wave height transformation model and a nearshore current model.

4.1 Wave height transformation model

The basic equation and the procedure of the present model for wave height transformation are based on those of the transformation model for directional random waves proposed by *Takayama et al.* (1991). Equation (2) expresses the energy equation of a wave component.

$$\left.\begin{aligned} &\frac{\partial (D_s V_x)}{\partial x} + \frac{\partial (D_s V_y)}{\partial y} + \frac{\partial (D_s V_\theta)}{\partial \theta} = -D', \\ &D_s = S(f,\theta)\,\delta f\,\delta\theta, \\ &V_x = C_g \sin\theta,\ V_y = C_g \cos\theta, \\ &V_\theta = \frac{C_g}{C}\left(-\cos\theta \frac{\partial C}{\partial x} - \sin\theta \frac{\partial C}{\partial y}\right), \end{aligned}\right\} \quad (2)$$

where D_s is the wave energy, S is the directional wave spectral density, δf is the frequency band width, $\delta\theta$ is the directional band width, C_g is the group velocity, θ is the wave direction, C is the celerity, and D' is the wave energy dissipation rate.

Takayama et al. (1991) introduced a wave energy dissipation term into the *Karlsson's* model (1969), which is based on the balance of wave energy. Wave dissipation rate calculated by their model is proportional to the beach slope. Thus the calculated wave dissipation rate on a bar crest, where the beach slope is equal to zero, is equal to zero. However, wave energy is dissipated even on a bar crest in the field because waves break on the bar crest. Therefore their wave dissipation term is not adopted for the calculation of the wave transformation over a bar.

Dally et al. (1985) proposed a wave energy dissipation term for one-dimensional monochromatic waves. Because the calculation with their wave dissipation term can represent the wave height stabilization in a uniform depth, the term is suitable for the calculation of the wave transformation over a bar and a trough. Therefore we introduce the wave energy dissipation term proposed by *Dally et al.* (1985) in the present model after improving it.

Equation (3) expresses their wave energy dissipation term for one-dimensional monochromatic waves.

$$\frac{\partial (EC_g')}{\partial y} = \frac{K'}{h}\left(EC_g' - E_s C_g'\right), \quad (3)$$

where E is the wave energy, C_g' is the group velocity of the wave, K' is a dimensionless coefficient, h is the water depth, and E_s is the wave energy where the wave height is stable after wave breaking. The stable wave height, H_s, is expressed as Eq.(4) with a dimensionless coefficient, Γ'.

$$H_s = \Gamma' \cdot h. \qquad (4)$$

Modifications of Eqs. (3) and (4) yield Eqs. (5) and (6) for directional random waves.

$$\left.\begin{aligned} &\frac{\partial(D_s V_x)}{\partial x} - \frac{\partial(D_s V_y)}{\partial y} + \frac{\partial(D_s V_\theta)}{\partial \theta} = -\frac{K}{h}\left(D_s C_g - D_s \frac{E_s}{E} C_g\right), \\ &E_s = \frac{1}{16}\rho g (H_{1/3})_s^2, \end{aligned}\right\} \qquad (5)$$

$$(H_{1/3})_s = \Gamma \cdot h, \qquad (6)$$

where $(H_{1/3})_s$ is the stable significant wave height and Γ is a dimensionless coefficient.

Although *Dally et al.* (1985) assumed that K and Γ are constant, wave energy dissipation in the surf zone is affected by the beach slope as they mentioned. Because beach slopes vary widely from 1/10 to -1/10 along the HORF, we assume that K and Γ are the functions of the beach slope, $\tan\beta$, and express them with Eqs.(7) and (8). These functions are obtained on the basis of the calculations of the wave height transformation in the surf zone for offshore wave steepness of 0.02 by *Goda* (1975).

$$\left.\begin{aligned} &K = 1.7 \cdot 10^{\alpha}, \\ &\alpha = -0.857 \log_{10}(1/\tan\beta) + 0.219, \end{aligned}\right\} \qquad (7)$$

$$\Gamma = -0.14 \log_{10}(1/\tan\beta) + 0.56. \qquad (8)$$

A significant wave height, $H_{1/3}$, and a principal wave direction, θ_p, are calculated by

$$\left.\begin{aligned} &H_{1/3} = 4.0\sqrt{m_0}, \\ &m_0 = \int_0^{\infty} \int_{-\pi/2}^{\pi/2} D_s \, d\theta \, df, \end{aligned}\right\} \qquad (9)$$

$$\theta_p = \int_0^{\infty} \int_{-\pi/2}^{\pi/2} \theta \cdot D_s \, d\theta \, df / m_0. \qquad (10)$$

4.2 Nearshore current model

a. Basic equations with momentum fluxes due to mass transport under bores in the surf zone

Mass transport due to waves is usually neglected in a previous model for nearshore current because the effect of the mass flux calculated with a formula for unbroken waves to nearshore current is small (*Yamaguchi et al.*, 1983). However, a mass flux due to bores in the surf zone is several times of that calculated with the formula for unbreaken waves (*Nadaoka and Kondoh*, 1982). It means that a momentum flux due to mass transport under bores is much greater than that under unbroken waves because the momentum flux is proportional to the square of the mass transport velocity. Therefore we consider the momentum fluxes due to mass transport under bores are significant for a longshore current distribution, and introduce them into a previous model.

The basic equations of a typical previous model for nearshore current (see, *e.g.*, *Nishimura*, 1988) are expressed as

$$\frac{\partial \overline{\eta}}{\partial t} + \frac{\partial (h + \overline{\eta}) U}{\partial x} + \frac{\partial (h + \overline{\eta}) V}{\partial y} = 0, \qquad (11)$$

$$\left.\begin{aligned}
&\frac{\partial U}{\partial t}+U\frac{\partial U}{\partial x}+V\frac{\partial U}{\partial y}+F_x-L_y+R_x+g\frac{\partial \overline{\eta}}{\partial x}=0,\\
&\frac{\partial V}{\partial t}+U\frac{\partial V}{\partial x}+V\frac{\partial V}{\partial y}+F_y-L_y+R_y+g\frac{\partial \overline{\eta}}{\partial y}=0,\\
&R_x=\frac{1}{\rho(h+\overline{\eta})}\left(\frac{\partial S_{xx}}{\partial x}+\frac{\partial S_{yx}}{\partial y}\right), \qquad R_y=\frac{1}{\rho(h+\overline{\eta})}\left(\frac{\partial S_{xy}}{\partial x}+\frac{\partial S_{yy}}{\partial y}\right),\\
&L_x=\frac{\partial}{\partial x}\left(\varepsilon\frac{\partial U}{\partial x}\right)+\frac{\partial}{\partial y}\left(\varepsilon\frac{\partial U}{\partial y}\right), \qquad L_y=\frac{\partial}{\partial x}\left(\varepsilon\frac{\partial V}{\partial x}\right)+\frac{\partial}{\partial y}\left(\varepsilon\frac{\partial V}{\partial y}\right),
\end{aligned}\right\} \quad (12)$$

where $\overline{\eta}$ is the elevation of the mean water level, t is the time, and U and V are the depth and time-averaged velocities in x-direction and y-direction, respectively. The values of F_x and F_y are the bottom friction terms, L_x and L_y are the lateral mixing terms, ρ is the density of the sea water, S_{xx}, S_{xy} and S_{yy} are the radiation stress components, and ε is a lateral mixing coefficient. Subscripts x and y denote the values in x-direction and y-direction, respectively.

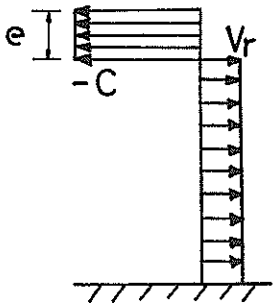

Figure 12 Definition sketch of the vertical distribution of the cross-shore velocity in the surf zone by *Svendsen* (1984).

To calculate the momentum fluxes due to mass transport under bores, we utilize the assumption of the vertical distribution of the cross-shore velocity in the surf zone in a steady two-dimensional situation proposed by *Svendsen* (1984); his assumption is shown in **Figure 12.** He assumed that the water near the surface is transposed onshoreward with the thickness of a bore, e, at the speed of wave celerity, $-C$, and that the return flow at the velocity of V_r exists below the onshoreward current.

Now we focus on the cross-shore flux of the longshore momentum in the surf zone, M_w. First, we assume that the mass of water transported onshoreward near the water surface returns offshoreward only through the return flow. This assumption is expressed as

$$\int_{d_{tr}}^{\eta} V_u(z)\cos\theta_p dz+V_l(d_{tr}+h)=0, \qquad (13)$$

where T is the wave period, η is the elevation of the water surface, d_{tr} is the elevation of the wave trough, $V_u(z)$ is the time-averaged velocity in the wave direction at the elevation of z over the wave

trough, V_l is the depth and time-averaged cross-shore velocity between the wave trough and the bottom. The value of $V_u(z)$ is equal to $-C$ in a bore, and is equal to V_r below the bore. The value of V_l is equal to $V_r\cos\theta_p$.

If the absolute value of the longshore momentum transported onshoreward in a bore is equal to that transported offshoreward below the bore, bores do not affect the cross-shore flux of the longshore momentum. However, the absolute value of the longshore momentum transported onshoreward is larger than that transported offshoreward owing to the oblique propagation of bores. Thus the cross-shore flux of the longshore momentum in the surf zone is affected by bores.

The cross-shore flux of the longshore momentum in the surf zone, M_w, is expressed as

$$M_w=\frac{\rho}{T}\int_0^T\int_{d_{tr}}^{\eta}\left[\left\{U+(V_u(z)+v_m(z)\cos\sigma t)\sin\theta_P\right\}\cdot\right.$$
$$\left.\left\{V+(V_u(z)+v_m(z)\cos\sigma t)\cos\theta_P\right\}\right]dzdt$$
$$+\frac{\rho}{T}\int_0^T\int_{-h}^{d_{tr}}\left[(U+v_m(z)\cos\sigma t\sin\theta_P)\cdot\right.$$
$$\left.(V+V_l+v_m(z)\cos\sigma t\sin\theta_P)\right]dzdt, \qquad (14)$$

where $v_m(z)$ is the maximum orbital velocity at z and σ is the angular frequency.
Equation (14) becomes

$$M_w=\frac{\rho}{T}\int_0^T\left|\int_{d_{tr}}^{\eta}UVdz+\int_{-h}^{d_{tr}}UVdz\right.$$
$$+\int_{d_{tr}}^{\eta}U\cdot V_u(z)\cos\theta_P dz+\int_{-h}^{d_{tr}}U\cdot V_l dz$$
$$+\int_{d_{tr}}^{\eta}v_m^2(z)\cos^2\sigma t\sin\theta_P\cos\theta_P dz$$
$$+\int_{-h}^{d_{tr}}v_m^2(z)\cos^2\sigma t\sin\theta_P\cos\theta_P dz$$
$$\left.+\int_{d_{tr}}^{\eta}\left(Vu^2(z)+V\cdot V_u(z)\right)\sin\theta_P\cos\theta_P dz\right|dt. \qquad (15)$$

The first term and the second term in the right-hand side of Eq.(15) is included in the previous model. The sum of the third term and the fourth term in the right-hand side is equal to zero because the mass of water transported onshoreward near the water surface returns offshoreward only through the return flow. The sum of the fifth term and sixth term expresses the radiation stress, which is included in the previous model. The seventh term expresses the cross-shore flux of the longshore momentum due to mass transport under bores, M_{bl}. When we assume that the return flow over the wave trough is negligible, the value of M_{bl} is expressed as Eq.(16) with the introduction of the fraction of breaking waves, P_b.

$$M_{bl}=P_b\cdot e\cdot(-C\cos\theta_p+V)\cdot C\sin\theta_p. \qquad (16)$$

The thickness of a bore, e, is expressed as Eq.(17) by *Svendsen* (1984).

$$e=C_A\cdot H^2/L, \qquad (17)$$

where C_A is called as the surface roller area parameter, H is the wave height and L is the wave length.

The cross-shore flux of the cross-shore momentum due to mass transport under bores, M_{b2}, and the longshore flux of the longshore momentum, M_{b3}, are obtained as the value M_{bl}; these are described by

$$M_{b2}=P_b\cdot e\cdot C^2\cos^2\theta_p+(d_{tr}+h)\cdot V_l^2, \qquad (18)$$

$$M_{b3}=P_b\cdot e\cdot (C\sin\theta_p+2U)\cdot C\sin\theta_p, \qquad (19)$$

The value of V_l is expressed as Eq.(20), which is derived by *Kuriyama*(1991) on the basis of the *Svendsen*'s model (1984).

$$V_l=\left(C\frac{m_0}{h^2}+P_b\cdot C_A\cdot\frac{H_{l13}^2}{h\,T_{1/3}}\right)\cdot\cos\theta_p. \qquad (20)$$

Finally, the horizontal momentum equation in the present model for nearshore current, which contains the momentum fluxes due to mass transport under bores, is represented by

$$\left.\begin{aligned}
&\frac{\partial U}{\partial t}+U\frac{\partial V}{\partial x}+V\frac{\partial U}{\partial y}+F_x-L_x+R_x+g\frac{\partial\bar{\eta}}{\partial x}+M_x=0,\\
&\frac{\partial V}{\partial t}+U\frac{\partial V}{\partial x}+V\frac{\partial V}{\partial y}+F_y-L_y+R_y+g\frac{\partial\bar{\eta}}{\partial y}+M_y=0,\\
&M_x=\frac{1}{\rho(h+\bar{\eta})}\left(\frac{\partial M_{b3}}{\partial x}+\frac{\partial M_{b1}}{\partial y}\right), \qquad M_y=\frac{1}{\rho(h+\bar{\eta})}\left(\frac{\partial M_{b1}}{\partial x}+\frac{\partial M_{b2}}{\partial y}\right).
\end{aligned}\right\} \qquad (21)$$

b. Fraction of breaking waves

We assume that the fraction of breaking waves is a function of wave height-water depth ratio as *Thornton and Guza* did (1983), and represent it by Eq.(22) with a dimensionless coefficient, γ. The value of γ is the wave height-water depth ratio that is constant in the surf zone; we consider it is the value where all waves are broken.

$$P_b=\{H_{1/3}/(\gamma\cdot h)\}^4. \qquad (22)$$

Thornton and Guza (1983) omitted the effect of the beach slope to the fraction of breaking waves. We, however, introduce the effect into the calculation of γ because the wave energy dissipation in the surf zone is affected by the beach slope. The value of γ is determined on the basis of the calculations of the wave height in the surf zone for offshore wave steepness of 0.02 by *Goda* (1975); the value of γ is expressed as

$$\gamma=0.68\exp(4.2\tan\beta). \qquad (23)$$

While bores are generated and developed in the offshore side of a bar crest, those bores decay in the onshore side of the bar crest. The bores, however, are visually observed not to start decaying from the bar crest. **Table 1** represents the onshore limits of breaker zones over bars, locations of the bar crests, the fractions of breaking waves on the bar crests and the onshore limits of bore propagation, which are the results of the visual observations conducted on November 2, 1991 and on February 26, 1992. The beach profiles over the bars and the troughs on November 2, 1991, and on February 26, 1992, are shown in **Figure 13(1)** and **13(2)**. Waves broke even in the onshore sides of the bar crests. Consequently bores propagated without decaying from the bar crests at the distances between 10m and 30m. Thus Eq.(22) is not adopted for the calculation of P_b in the onshore side of a bar crest.

Therefore we assume that the fraction of breaking waves in the onshore side of a bar crest decreases

Table 1 Breaking wave conditions over the bars on November 2, 1991 and on February 26, 1992.

Measurement time	Onshore limit of breaker zone over bar	Location of bar crest	Fraction of breaking waves on bar crest	Onshore limit of bore propagation
Nov. 2 ,1991				
9:20	P350m	P380m	83%	P310m
11:15	P350m	P380m	58%	P310m
13:25	P350m	P380m	49%	P310m
15:15	P345m	P380m	49%	P320m
Feb.26,1992				
9:40	P380m	P360m	84%	P290m
11:45	P350m	P360m	64%	P290m
13:45	P350m	P360m	73%	P290m

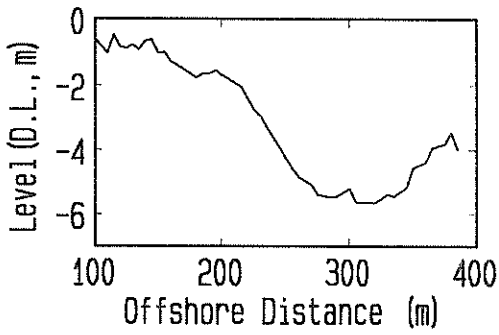

Figure 13(1) Beach profile on November 2, 1991.

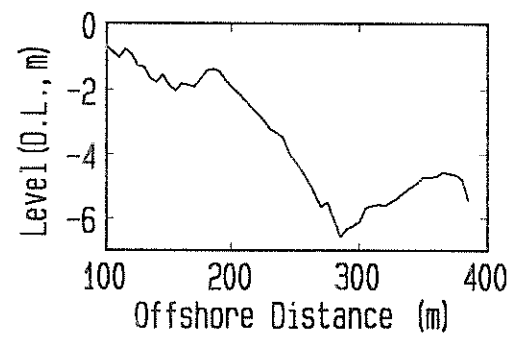

Figure 13(2) Beach profile on February 26, 1992.

onshoreward proportionally with the square of the offshore distance from the bar crest. The value of P_b in the onshore side of a bar crest is assumed to be given by Eq.(24); the coefficients of Eq.(24) is determined on the basis of the figures in **Table 1.**

$$P_b = (P_b)_{bar} - 0.014 \cdot (y - y_{bar} + 10)^2, \quad (24)$$

where $(P_b)_{bar}$ is the fraction of breaking waves at the bar crest. The units of y and y_{bar} in Eq.(24) are meter.

c. Surface roller area parameter

Svendsen (1984) treated the surface roller area parameter as a constant value of 0.9 on the basis of the Duncan's experimental data for breaking waves behind a hydrofoil. *Okayasu et al.* (1988) showed that the return flow velocities calculated with the value of 2.4 as the parameter agreed with the experimental data. *Shimizu et al.* (1992) obtained the values between 4 and 7 as the parameter on the basis of the field data. *Kuriyama* (1991) showed that the surface roller area parameter decreases from 4 to 2 onshoreward from the averaged wave breaking position, and suspected that the parameter decreases according to the decay of bores.

In a trough, the thickness of a bore is visually observed to decrease as the bore propagates with decaying. Thus we assume that the surface roller area parameter changes according to the development and decay of a bore as shown in **Figure 14.**

The development and decay of a bore is assumed to be proportional to the fraction of wave breaking; the maximum value of C_A is defined to be 4 on the basis of the field data obtained by *Kuriyama* (1991). Finally, the surface roller area parameter is expressed as

$$C_A=4.0 \cdot P_b. \qquad (25)$$

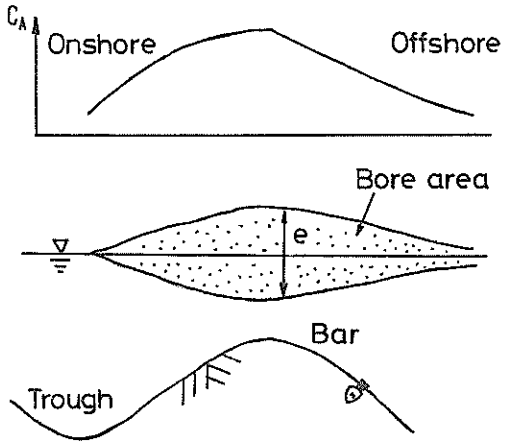

Figure 14 Definition sketch of the variations of thickness of bores and surface roller area parameter, C_A.

d. Radiation stress, bottom shear stress and lateral mixing

Radiation stresses of directional random waves are calculated by Eq.(26) proposed by *Yamaguchi*(1988).

$$\left.\begin{aligned} S_{xx}&=\int_0^{\infty}\int_{-\pi/2}^{\pi/2}\rho g\{\frac{C_g}{C}\sin^2\theta+(\frac{C_g}{C}-\frac{1}{2})\}D_s\,d\theta\,df,\\ S_{xy}=S_{yx}&=\int_0^{\infty}\int_{-\pi/2}^{\pi/2}\rho g\frac{C_g}{C}\cos\theta\sin\theta\,D_s\,d\theta\,df,\\ S_{yy}&=\int_0^{\infty}\int_{-\pi/2}^{\pi/2}\rho g\{\frac{C_g}{C}\cos^2\theta+(\frac{C_g}{C}-\frac{1}{2})\}D_s\,d\theta\,df. \end{aligned}\right\} \qquad (26)$$

Equation (27), which was proposed by *Nishimura*(1982), is used for the calculation of bottom shear stresses, F_x and F_y. The value of 0.005 are used as the friction coefficient, C_f; the value of 0.005 was obtained on the basis of the longshore current velocities and wave heights in the field with the previous model (*Kuriyama et al.*, 1992).

$$
\left.
\begin{aligned}
F_x &= \rho C_f \{(W+\frac{w_b^2}{W}\sin^2\theta_p)U-\frac{w_b^2}{W}\sin\theta_p\cos\theta_p V\}, \\
F_y &= \rho C_f \{\frac{w_b^2}{W}\sin\theta_p\cos\theta_p U-(W+\frac{w_b^2}{W}\cos^2\theta_p)V\}, \\
W &= \Big|\sqrt{U^2+V^2+w_b^2+2(U\sin\theta_p-V\cos\theta_p)w_b} \\
&\quad +\sqrt{U^2+V^2+w_b^2+2(U\sin\theta_p-V\cos\theta_p)w_b}\Big| / 2, \\
w_b &= 2\cdot v_m(-h)/\pi,\ v_m(-h)=\frac{\pi\cdot H_{1/3}}{T\sin(2\pi h/L)}.
\end{aligned}
\right\} \quad (27)
$$

The lateral mixing coefficient proposed by *Battjes*(1975) is used in the present model. This coefficient is given by

$$\epsilon = Mh\,(\frac{D}{\rho})^{1/3}, \qquad (28)$$

where D is the total wave energy dissipation rate and M is a dimensionless coefficient.

Lateral mixing is probably related to the turbulence in the water; the turbulence due to broken waves is much larger than that due to unbroken waves. Although the lateral mixing coefficient proposed by *Longuet-Higgins* (1970) is widely used, he did not consider wave breaking. Thus the coefficient proposed by Longuet-Higgins is considered to indicate the upper limit as *Battjes* mentioned (1975). In a trough, the actual rate of lateral mixing must be much smaller than that calculated with the coefficient proposed by Longuet-Higgins. On the contrary, the lateral mixing rate calculated with the coefficient proposed by Battjes probably agrees with the actual values because the coefficient proposed by Battjes is based on the wave energy dissipation by wave breaking. Thus we adopt the lateral mixing coefficient proposed by Battjes in the present model.

Nearshore currents are calculated with M=2, 5 and 10, and are compared with the measured values because the dimensionless coefficient, M, is not thoroughly investigated, and optimal M for nearshore current is unknown.

5. Model comparisons with measurements

5.1 Calculation conditions

Nearshore currents on March 24, 28 and April 4, 1989, are selected for the comparisons of the longshore current velocities calculated by the present model and by the previous model with the measured values. The reasons are as follows:

(a) Bars and troughs were formed.

(b) Waves broke over the bars.

(c) Topographic survey around the HORF, which has been carried out once or twice a year, was conducted on March 31, 1989. Beach profile changes between March 24 and April 4 were small.

Figure 15 shows the topographic map on March 31, 1989. **Figure 16** shows the beach profile along the HORF and the mean beach profile in the region between 100m and 300m from the HORF. The thick solid line and the thin solid line with short vertical lines indicate the beach profile along the HORF and the mean beach profile, respectively. The short vertical lines indicate the standard deviations of the beach profiles in the region between 100m to 300m from the HORF. The location of

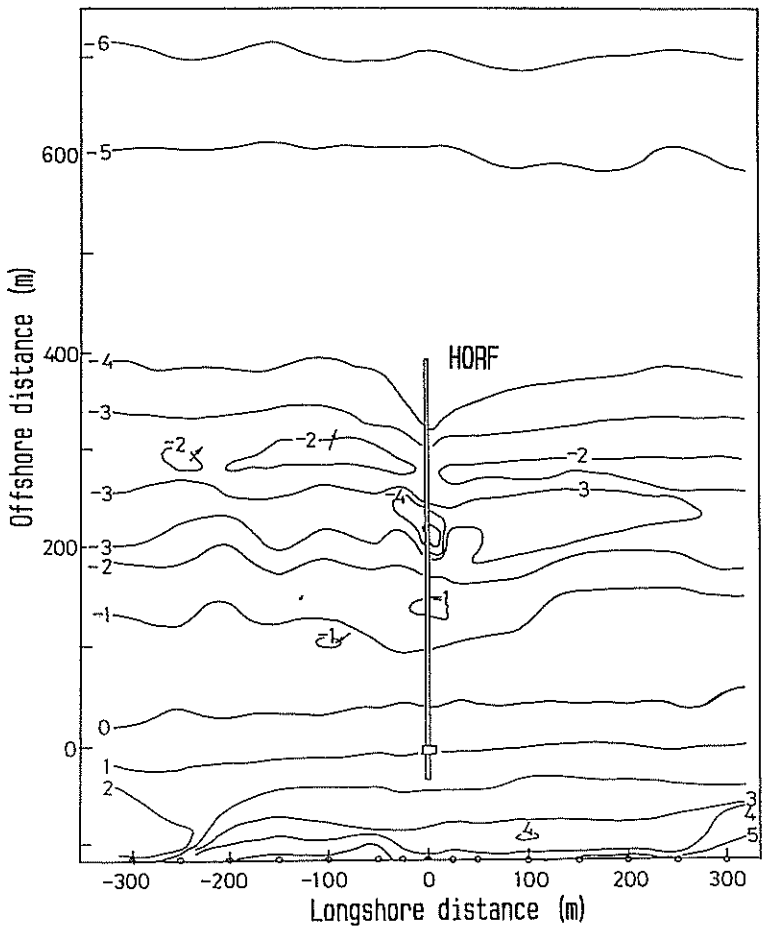

Figure 15 Topographic map on March 31, 1989.

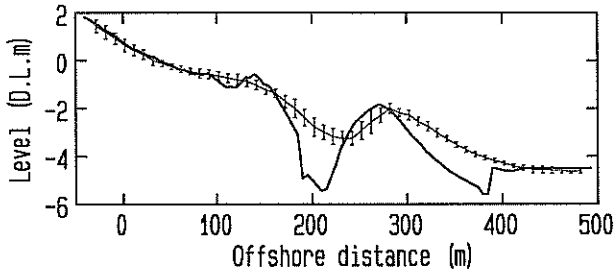

Figure 16 Beach profile along the HORF and mean beach profile in the region between 100m to 300m from the HORF.

the bar crest, the water depth at the bar crest and the location of the trough of the beach profile along the HORF agree with those of the mean beach profile although scours have occurred around the tip of

the HORF and P200m, where bridge piers are concentrated.

The calculation areas extend from the shorelines to y=650m, and from x=-320m to x=320m.

a. Wave height transformation

The grid distances in x-direction and y-direction are 10m. The numbers of frequency components and directional components are 10 and 35, respectively.

Wave heights, $(H_{1/3})_{ob}$, wave periods, $(T_{1/3})_{ob}$, principal wave directions, $(\theta_p)_{ob}$, and spreading parameters, $(s_{max})_{ob}$, at the offshore boundaries are listed in **Table 2**. The values of $(H_{1/3})_{ob}$ are calculated on the basis of the field data at the water depth of 23.4m. The values of $(T_{1/3})_{ob}$ are equal to the values at the water depth of 23.4m. The principal wave directions, $(\theta_p)_{ob}$, are calculated from the visual observations at the tip of the HORF with the graph of the wave direction of random waves due to refraction by *Goda and Suzuki* (1975). The spreading parameters in deep water are assumed to be 10; the values of $(s_{max})_{ob}$ are calculated with the graph of spreading parameter in shallow water by *Goda and Suzuki* (1975).

Table 2 Offshore boundary conditions.

Calculation date in 1989	$(H_{1/3})_{ob}$(m)	$(T_{1/3})_{ob}$(s)	θ_{ob}(degree)	$(Smax)_{ob}$
March 24	3.20	11.20	−20.0	90
March 28	3.00	8.86	−25.0	40
April 4	2.03	8.40	−10.0	45

The Bretschneider-Mitsuyasu frequency spectrum and the Mitsuyasu-type spreading function are given at the offshore boundaries.

A beach slope below 1/100 and that over 1/10 are replaced by 1/100 and 1/10, respectively, because Eqs.(7) and (8) are valid for the beach slope from 1/100 to 1/10.

b. Nearshore current

The nearshore currents in the surf zone are calculated by the ADI (Alternating Direction Implicit) method (see, *e.g., Horie et al.*, 1977; Nishimura, 1988). The grid distances in x-direction and y-direction are 10m, which are the same values in the wave transformation calculation. The time step is 0.4s. The number of the iterations is determined to be 4000.

The nearshore current velocities are assumed to be equal to zero at the offshore boundaries and at the shorelines. The nearshore current velocities and the mean water levels at the side boundaries are assumed to be equal to the values at internal grid points next to the side boundaries.

The longshore flux of the longshore momentum, M_{b3}, is neglected in the calculations of the nearshore currents on March 24, 28 and April 4 because the nearshore currents preliminarily calculated by the previous model are almost uniform alongshore.

5.2 Wave height

Figures 17(1) to **17(3)** show the predicted significant wave heights and the values measured at the HORF on March 24, 28 and April 4, respectively. The solid lines show the values predicted by the present model. The closed circles show the values measured before and after the measurements of longshore currents. The predicted values agree well with the measured values except for the data near the shorelines on March 28 and on April 4 .

The cause of the small disagreement of the measured values and the calculated values near the

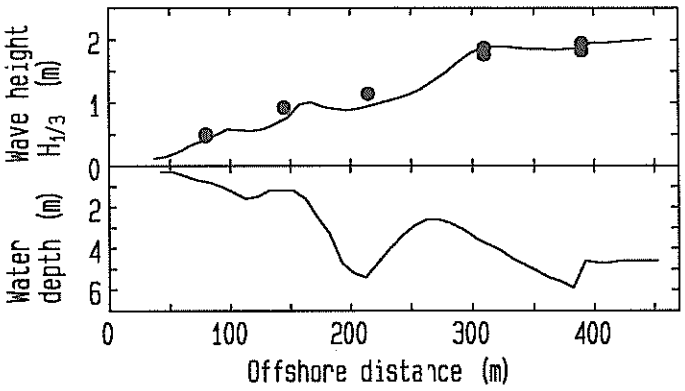

Figure 17(1) Comparison of significant wave heights calculated by the present model with the measured values on March 24, 1989.

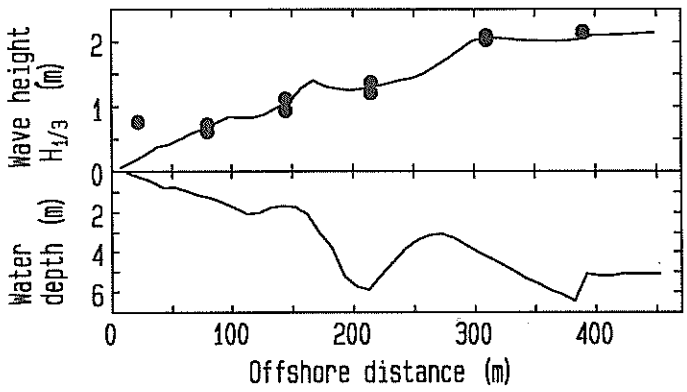

Figure 17(2) Comparison of significant wave heights calculated by the present model with the measured values on March 28, 1989.

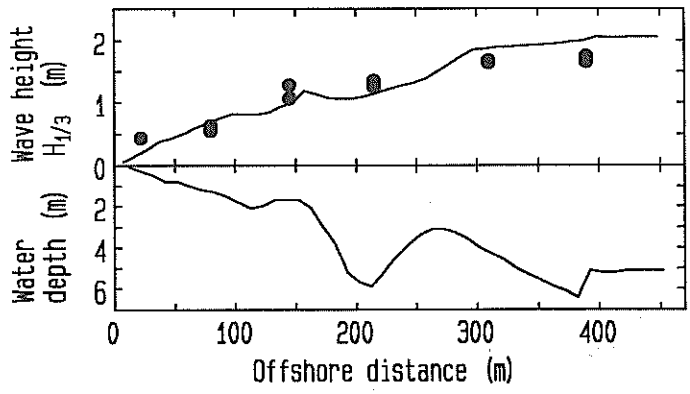

Figure 17(3) Comparison of significant wave heights calculated by the present model with the measured values on April 4, 1989.

shorelines is supposed to be wave setup and infragravity waves. When an offshore wave height is large, the amount of wave setup and the infragravity wave height are large near the shoreline; these phenomena were observed at the HORF by *Yanagishima and Katoh* (1990) and by *Nakamura et al.* (1992). Infragravity waves and wave setup, however, are not taken into account in the present model. The disregards of the two factors result in the disagreement of the calculated values and the measured values near the shorelines.

Although the effect of the offshore wave steepness to the wave energy dissipation in the surf zone is not included in the present model, the calculated values agree well with the measured values. The values of the offshore wave steepness on March 24, 28 and April 4 are between 0.013 and 0.022; the scattering of the offshore wave steepness around 0.02 is small. Thus the calculated values agree well with the measured values.

5.3 Nearshore current

Figure 18(1) shows the nearshore current on March 24, 1989, calculated by the present model with M=5, which will be shown to be optimal value for the nearshore current on March 24. The solid line in the right figure indicates the beach profile at x=0m, while the dashed line indicates the mean beach profile between x=−300m and x=−100m, and between x=100m and x=300m. Although the direction of the nearshore current in the trough between y=200m and y=300m changes slightly offshoreward at x=−50m, the nearshore current is almost uniform alongshore.

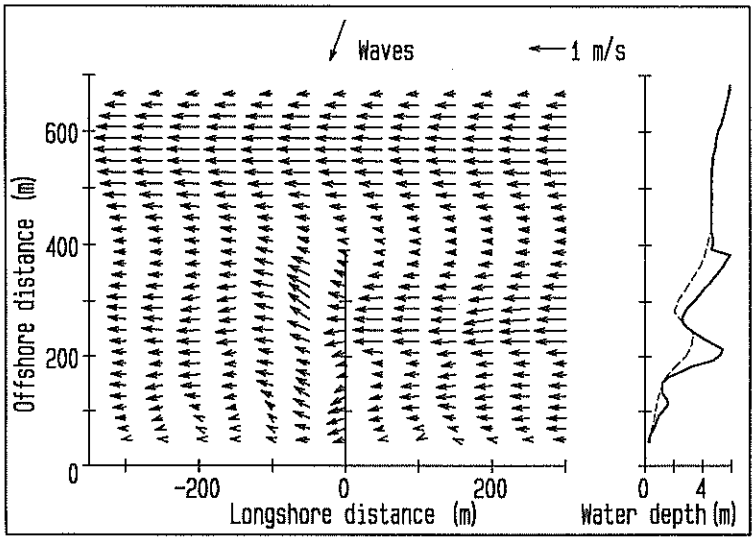

Figure 18(1) Nearshore current on March 24, 1989, calculated by the present model with M=5.

The comparisons between the longshore current velocities at x=0m calculated with M=2, 5 and 10 are shown in **Figure 18(2)**; the signs of the longshore current velocities are changed from minus to plus in this figure. The calculated values with M=5 seem to agree best with the measured values.

Figure 18(3) shows the comparisons between the longshore current velocities measured along the HORF and those calculated with M=5 by the present model and by the previous model. The longshore current distribution over the bar and the trough calculated by the present model agrees with the measured one although the calculated distribution by the previous model disagrees with the measured

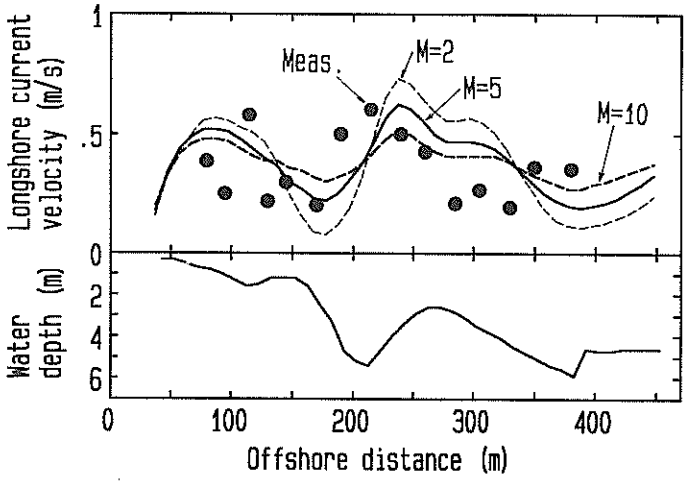

Figure 18(2) Longshore current velocities on March 24, 1989, calculated by the present model with M=2, 5 and 10.

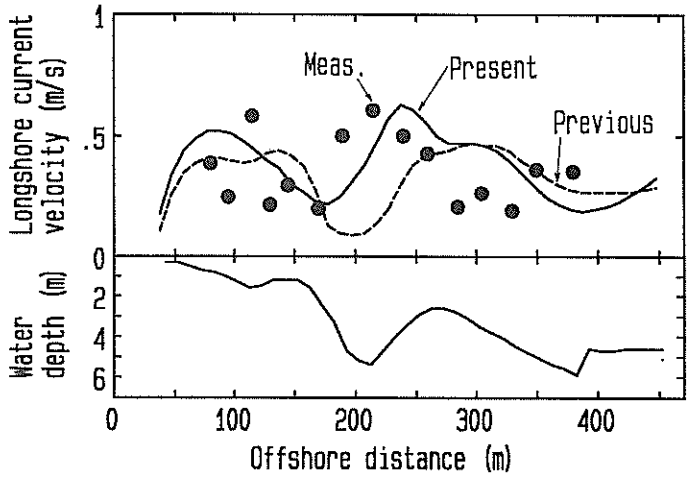

Figure 18(3) Comparisons of the measured longshore current velocities on March 24, 1989, with those calculated with M=5 by the present model and by the previous model.

one especially at the trough. The differences between the calculated values by the present model and those by the previous model are small in the offshore side of the bar crest; both values are larger than the measured ones in the area between P330m and P280m. In the onshore side of the bar crest, however, the values calculated by the present model and the measured values increase onshoreward although the values calculated by the previous model decrease. As a result, the longshore current distribution calculated by the present model has a peak velocity in the onshore side of the bar crest as the measured one, while the distribution calculated by the previous model has a peak velocity in the offshore side of the bar crest.

In the secondary surf zone, the longshore current distribution calculated by the present model agrees roughly with the measured one. However, the agreement of the calculated one with the measured one

in the secondary surf zone is worse than that over the bar and the trough.

Figure 19(1) shows that the nearshore current on March 28, 1989, calculated by the present model with M=5. This nearshore current is also almost uniform alongshore although the direction of the nearshore current in the trough changes slightly at x=-50m.

The comparisons between the longshore current velocities calculated with M=2, 5 and 10 are shown in **Figure 19(2)**. The value of 5 is also optimal M for the nearshore current on March 28.

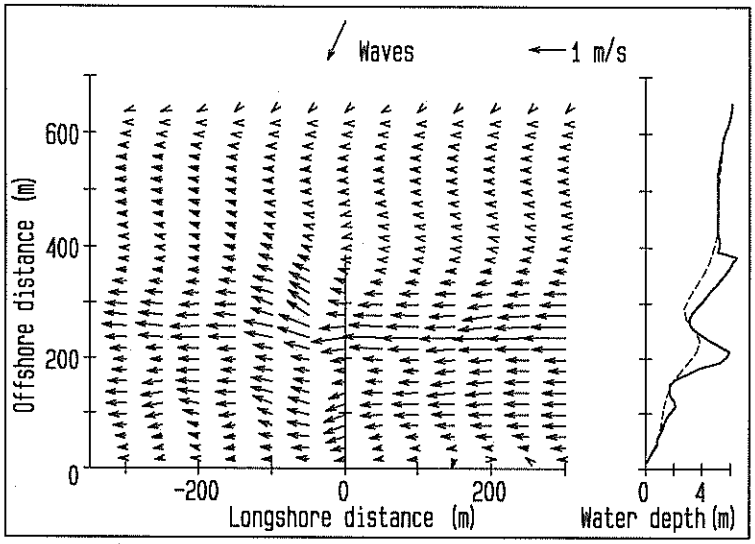

Figure 19(1) Nearshore current on March 28, 1989, calculated by the present model with M=5.

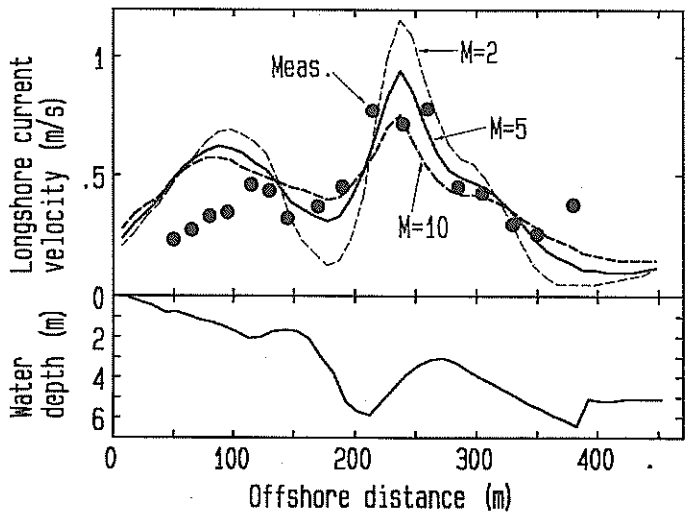

Figure 19(2) Longshore current velocities on March 28, 1989, calculated by the present model with M=2, 5 and 10.

Figure 19(3) shows the comparisons between the longshore current velocities measured at the HORF and those calculated with M=5 by the present model and by the previous model. In the offshore side of the bar crest, the values calculated by the present model and by the previous model increase onshoreward; the values calculated by the present model agree with the measured values slightly better than those by the previous model. In the onshore side of the bar crest, the values calculated by the present model and the measured values increase onshoreward although the values calculated by the previous model decrease. Consequently the longshore current velocities over the trough calculated by the present model agree well with the measured values although the values calculated by the previous model disagree with the measured values.

In the secondary surf zone, the dimensionless profile of the longshore current calculated by the present model agrees roughly with the measured one. However, the values calculated by the present model are larger than the measured ones.

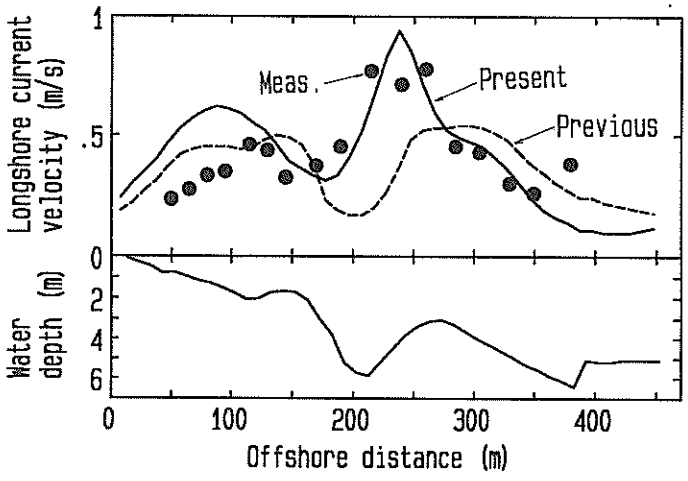

Figure 19(3) Comparisons of the measured longshore current velocities on March 28, 1989, with those calculated with M=5 by the present model and by the previous model.

Figure 20(1) shows the nearshore current on April 4, 1989, calculated by the present model with M=10. A small rip current appears at x=-50m; the rip current is supposed to affect the longshore current at x=0m.

Figure 20(2) shows the comparisons between the longshore current velocities calculated with M=2, 5 and 10. The distribution calculated with M=10 best agrees with the measured one, while the distributions on March 24 and 28 calculated with M=5 best agree with the measured ones.

Figure 20(3) shows the comparisons between the longshore current velocities measured at the HORF and those calculated with M=10 by the present model and by the previous model. In the offshore side of the bar crest, the differences between the values calculated by the present model and those calculated by the previous model are very small; both values agree with the measured values. On

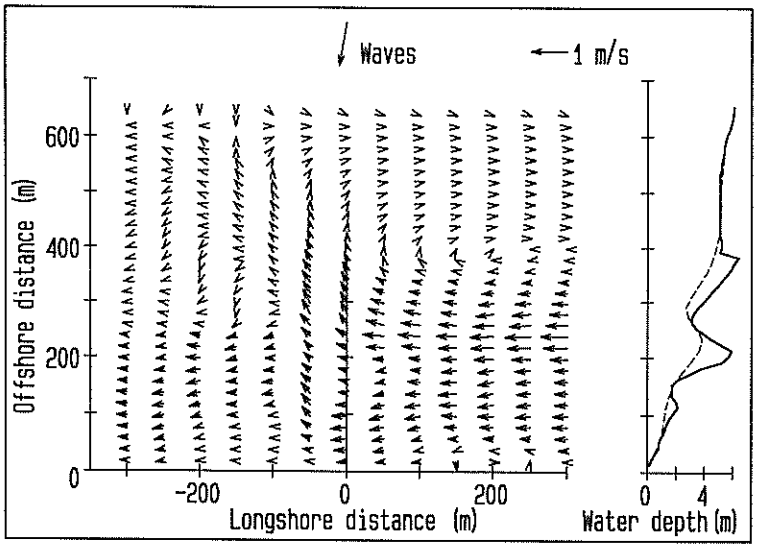

Figure 20(1) Nearshore current on April 4, 1989, calculated by the present model with M=10.

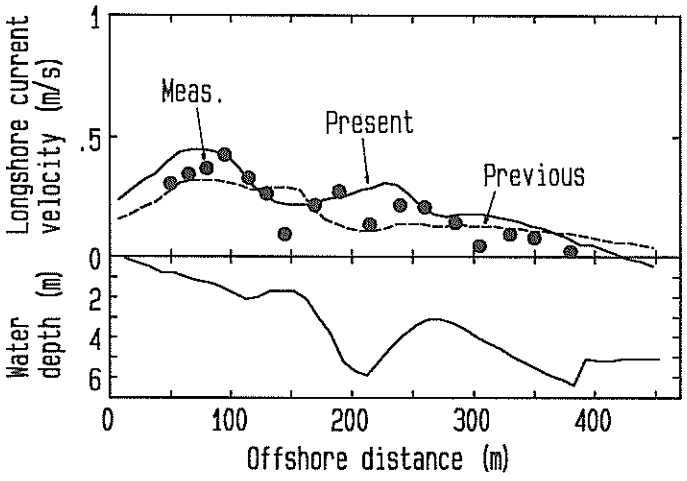

Figure 20(2) Longshore current velocities on April 4, 1989, calculated by the present model with M=2, 5 and 10.

the contrary, the differences are a little large in the onshore side of the bar crest. The values calculated by the present model and the measured values increase onshoreward although the values calculated by the previous model slightly decrease. Consequently the longshore current distribution over the bar and the trough calculated by the present model agrees with the measured one better than that calculated by the previous model although the measured value at P210m agrees with the value calculated by the previous model.

In the secondary surf zone, the longshore current profile calculated by the present model agrees with the measured one.

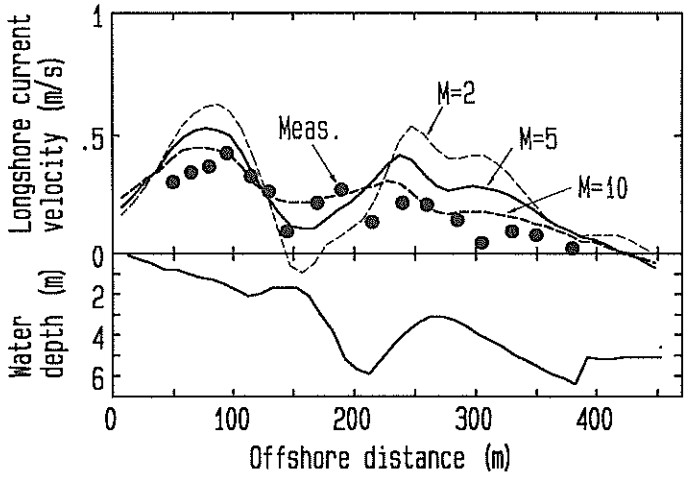

Figure 20(3) Comparisons of the measured longshore current velocities on April 4, 1989, with those calculated M=10 by the present model and by the previous model.

6. Discussion

Let us assume that an incident wave angle and the longshore current velocity are positive. In the onshore side of a bar crest, the cross-shore flux of the longshore momentum due to mass transport under bores decreases onshoreward owing to the bore decay. This decrease means that the cross-shore flux of the longshore momentum transported into a unit volume is larger than that transported out of the volume. Consequently the longshore current velocities calculated by the present model are larger than those calculated by the previous model.

On the contrary, in the offshore side of the bar crest, the cross-shore flux of the longshore momentum due to mass transport under bores increases onshoreward owing to the bore development. Thus the longshore current velocities calculated by the present model are smaller than those calculated by the previous model.

As a result, the longshore current distribution calculated by the present model has a peak velocity in the onshore side of the bar crest as 85 percent of the distributions measured at the HORF. This agreement of the calculated distribution by the present model with the measured ones confirms the significance of the momentum fluxes due to mass transport under bores.

Although the longshore current distribution calculated by the present model has a peak velocity in the onshore side of the bar crest, 15 percent of the measured longshore current distributions have peak velocities in the offshore sides of bar crests.

To reveal a generation mechanism of the latter distribution, which has a peak velocity in the offshore side of a bar crest, we investigate the relationships between the offshoreward distance from y_{bar} to y_{peak} and H_0/L_0, the beach slope in the offshore side of the bar crest, tan β_{bar}, and h_{bar}. However, there are no correlations between them as shown in **Figures 21(1)** to **21(3)**.

We suppose that one of the causes of the generation of the latter distribution is bore decaying in the offshore side of the bar crest. When *Whitford and Thornton* (1988) measured the latter distribution, the fraction of breaking waves decreased onshoreward even in the offshore side of the bar crest. The

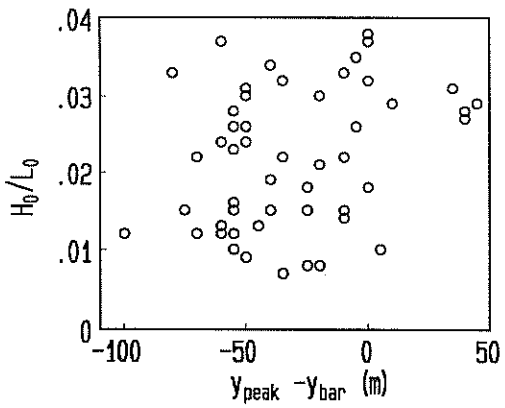

Figure 21(1) Relationship between y_{peak}-y_{bar} and H_0.

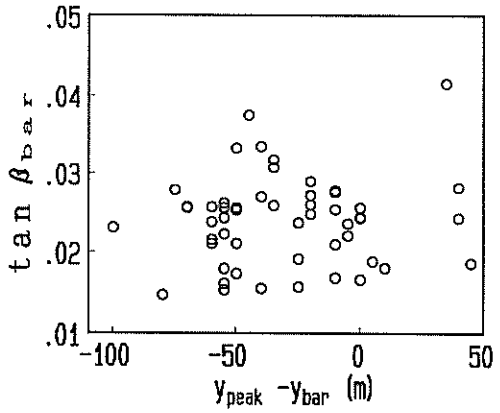

Figure 21(2) Relationship between y_{peak}-y_{bar} and tan β_{bar}.

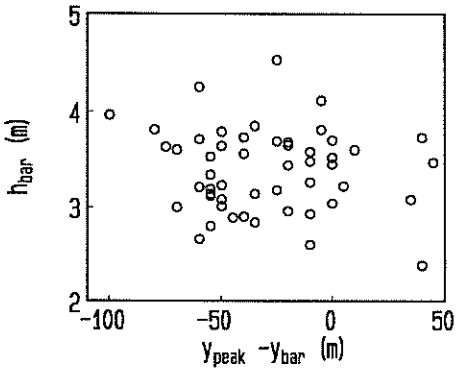

Figure 21(3) Relationship between y_{peak}-y_{bar} and h_{bar}.

decrease of the fraction of the breaking waves probably reflects bore decaying. The cross-shore flux of the longshore momentum due to mass transport under bores in the area where bores decay makes a longshore current velocity larger than that due to the cross-shore gradient of radiation stress, which is calculated by the previous model. The distribution of the longshore current due to the cross-shore gradient of radiation stress already has a peak velocity in the offshore side of the bar crest. Consequently the longshore current distribution when a bore starts decaying in the offshore side of the bar crest has a peak velocity in the offshore side of the bar crest.

The frequency of the bore decaying in the offshore side of a bar crest is supposed to be small because the percentage of the measured distribution that has a peak velocity in the offshore side of a bar crest is only fifteen percent. The cause of the bore decaying in the offshore side of a bar crest, which is unknown, should be investigated to widen the application of the present model.

The longshore current velocities near the shorelines calculated by the present model are larger than the measured ones. The float for measurements sometimes touched the bottom near shoreline when

wave trough depth is small, even though we shortened the length of the line between the float and the identification buoy at the small water depth. The inaccuracy of the measurements near shoreline results in the disagreement of the calculated longshore current velocities with the measured ones near the shorelines.

Although we omitted the longshore flux of the longshore momentum due to mass transport under bores, M_{b3}, in the calculation of nearshore current by the present model, the value of M_{b3} is necessary for the calculation of nearshore current where longshore topographic inhomogeneities are large. The longshore mass flux due to mass transport under bores, $\rho eC\sin\theta_p$, which is concentrated near the water surface, should also be included in the continuity equation although the calculation of the nearshore current would be complicated.

7. Summary and Conclusions

Field measurements of longshore current have been carried out at Hazaki Oceanographical Research Facility (HORF) when waves broke over bars. A spherical float having a diameter of 0.2m was used to measure nearshore current velocities at 1m below the water surface. This measurement method with the float was confirmed to be useful by the calibrations with an electromagnetic current meter.

Eighty-five percent of the measured longshore current distributions have peak velocities in the onshore sides of the bar crests, while fifteen percent of the measured distributions have peak velocities in the offshore sides of the bar crests.

A numerical model for nearshore current in the surf zone has been developed. First, we developed a wave height transformation model in the surf zone to calculate the driving forces of nearshore current such as radiation stresses. The basic equations of the present model are based on those of the transformation model for directional random waves proposed by *Takayama et al.* (1991). We introduced the wave dissipation term proposed by *Dally et al.*(1985) in the present model after improving it. The significant wave heights calculated by the present model agree well with the field data.

The developed numerical model for nearshore current contains the momentum fluxes due to mass transport under bores in the surf zone. To calculate the momentum fluxes due to mass transport under bores, we utilized the assumption of the vertical distribution of the cross-shore velocity in the surf zone proposed by *Svendsen* (1984) with the fraction of breaking waves and the surface roller area parameter, which determines the thickness of a bore. The fraction of breaking waves was assumed to be a function of wave height-water depth ratio in the offshore side of a bar crest, and to decrease onshoreward proportionally with the square of the offshore distance from the bar crest in the onshore side of the bar crest. We assumed that the surface roller area parameter varies according to the development and decay of a bore, and expressed the parameter with the fraction of wave breaking. The lateral mixing was calculated with the coefficient proposed by *Battjes*(1975).

The nearshore currents when the nearshore topographies around the HORF were known were calculated. The longshore current velocity distributions calculated by the present model, which have peak velocities in the onshore sides of the bar crests, agree with the measured ones, while the distributions calculated by a previous model disagree with the measured ones. This agreement of the distribution calculated by the present model with the measured one confirms the significance of the momentum fluxes due to mass transport under bores.

Although the longshore current distributions calculated by the present model have peak velocities in the onshore sides of bar crests, fifteen percent of the measured longshore current distributions have

those in the offshore sides of the bar crests. One of the causes of the generation of the latter distribution is supposed to be bore decaying in the offshore side of a bar crest.

Acknowledgements

We are grateful to the following individuals for their great contributions on the field measurements, which are sometimes very hard: Mr. Shin-ichi Yanagishima and Mr. Satoshi Nakamura, members of the Littoral Drift Laboratory, Port and Harbour Research Institute (PHRI), Mr. Hiroyuki Murakami and Mr. Tomoyoshi Isogami, former members of the Littoral Drift Lab., and Mr. Tatsuro Usui and Mr. Takayuki Tsuchiya, members of ECOH Inc. Further acknowledgement is extended to Dr. Kazumasa Katoh, the Chief of the Littoral Drift Lab., and Dr. Setsuo Noda, the Deputy Director General, PHRI, for their useful comments that improved this paper. Kashima Port Construction Office of the Second District Port Construction Bureau, Ministry of Transport, and the Marine Observation Lab., PHRI, provided the offshore wave data.

(Received on June 29, 1993)

References

1) Allender J.H. and J.D. Ditmars (1981): Field measurements of longshore currents on a barred beach, *Coastal Eng.*, 5, pp.295-309.
2) Battjes J.A. (1975): Modeling of turbulence in the surf zone, *Symp. on Modeling Techniques*, ASCE, pp.1050-1061.
3) Church J.C. and E.B. Thornton (1992): Bottom stress modification by breaking waves within a longshore current model, *Proc. 23rd Coastal Eng. Conf.*, ASCE, pp.3012-3025.
4) Dally W.R., R.G. Dean and R.A. Dalrymple (1985): Wave height variation across beaches of arbitrary profile, *J. Geophys. Res.*, Vol.90, No.C6, pp.11,917-11,927.
5) Goda Y. (1975): Irregular wave deformation in the surf zone, *Coastal Eng. in Japan*, Vol.18, pp.13-26.
6) Goda Y. and Y. Suzuki (1975): Computation of refraction and diffraction of sea waves with Mitsuyasu's directional spectrum, *Tech. Note Port and Harbour Res. Inst.*, No.230, 45p. (*in Japanese*)
7) Greenwood B. and D.J. Sherman (1986): Longshore current profiles and lateral mixing across the surf zone of a barred nearshore, *Coastal Eng.*, 10, pp.149-168.
8) Horie T., S. Sato and K. Murakami (1977): Boundary treatment on tidal computation, *17th Congress of the International Association for Hydraulic Research*, Vol.2, pp.359-366.
9) Karlsson T. (1969): Refraction of continuous ocean wave spectra, *J. Waterways and Harbors Div., Proc. of the ASCE*, Vol.95, No.WW4, pp.437-448.
10) Komar P.D. (1983): Nearshore currents and sand transport on beaches, *physical Oceanography of Coastal and Shelf Seas* (ed. by B. Johns), Elsevier, pp. 67-109.
11) Kuriyama Y. (1991): Investigation of cross-shore sediment transport rates and flow parameters in the surf zone using field data, *Rep. of the Port and Harbour Res. Inst.*, Vol.30, No.2, pp.3-58.
12) Kuriyama Y., K. Katoh and Y. Ozaki (1992): Longshore current distributions, bottom profiles and waves, *Proc. Coastal Eng.*, JSCE, Vol.39, pp.196-200. (*in Japanese*)
13) Larson M. and N.C. Kraus (1991): Numerical model of longshore current for bar and trough beaches, *J. Waterway, Port, Coastal, and Ocean Eng.*, Vol.117, No.4, ASCE, pp.326-347.
14) Longuet-Higgins (1970): Longshore current generated by obliquely incident waves, 1&2, *J.*

Geophys. Res.,Vol.75, No.33, pp.6778-6801.

15) Nadaoka K. and T. Kondoh (1982): Laboratory measurements of velocity field structure in the surf zone by LDV, *Coastal Eng. in Japan*, Vol.25, pp.125-146.

16) Nakamura S., K. Katoh and N. Ikeda (1992): Generation of infragravity waves in breaking process of wave groups, *Proc. 23rd Coastal Eng.* Conf., ASCE, pp.990-1005.

17) Nishimura H. (1982): Numerical simulation of the nearshore circulation, *Proc. 29th Japanese Conf. on Coastal Eng.*, JSCE, pp.333-337. (*in Japanese*)

18) Nishimura H. (1988): Computation of nearshore current, *Nearshore Dynamics and Coastal Process - Theory, Measurements and Predictive Models* - (ed. by K. Horikawa), University of Tokyo Press, pp.271- 291.

19) Shimizu T., M. Tsuru and A. Watanabe (1992): Numerical prediction model of long-term beach evolution, *Proc. Coastal Eng.*, JSCE, Vol.39, pp.416- 420. (*in Japanese*)

20) Svendsen I.A. (1984): Mass flux and undertow in a surf zone, *Coastal Eng.*, 8, pp.347-365.

21) Takayama T., N. Ikeda and T. Hiraishi (1991): Practical computation method of directional random wave transformation, *Rep. of the Port and Harbour Res. Inst.*, Vol.30, No.1, pp.21-67. (*in Japanese*)

22) Thornton E.B. and R.T. Guza (1983): Transformation of wave height distribution, *J. Geophys. Res.*, Vol.88, No.C10, pp.5925-5938.

23) Whitford D.J. and E.B. Thornton (1988): Longshore current forcing at a barred beach, *Proc. of 21st Coastal Eng. Conf.*, ASCE, pp.77-90.

24) Yamaguchi M., H. Tanabe, Y. Nishioka (1983): A numerical solution of nearshore currents taking account of wave-induced mass flux, *Proc. 30th Japanese Conf. on Coastal Eng.* JSCE, pp.480-484. (*in Japanese*)

25) Yamaguchi M. (1988): A numerical model of nearshore currents due to irregular waves, *Proc. of 21st Coastal Eng. Conf.*, ASCE, pp.1113- 1126.

26) Yanagishima S. and K. Katoh (1990): Field observation on wave set-up near the shoreline, *Proc. 22nd Coastal Eng. Conf.*, ASCE, pp.95-108.

List of Main Symbols

C :Celerity of a wave component
C_A :Surface roller area parameter
C_f :Friction coefficient
C_g :Group velocity of a wave component
C_g' :Group velocity of a monochromatic wave
D :Total dissipation rate of wave energy
D' :Energy Dissipation rate of a wave component
D_s :Energy of a wave component
d_{tr} :Elevation of wave trough
E :Total wave energy
E_s :Total wave energy where wave height is stable after wave breaking
e :Thickness of a bore
F_x, F_y :Bottom frictions
H :Wave height
H_0 :Significant wave height at the water depth of 23.4m
$H_{1/3}$:Significant wave height

$(H_{1/3})_{ob}$:Significant wave height at the offshore boundary
$(H_{1/3})_s$:Significant wave height where wave height is stable after wave breaking
h :Water depth
h_{bar} :Water depth at a bar crest
h_{trough} :Water depth at a trough
L :Wave length
L_x, L_y :Lateral mixing terms
M :Dimensionless coefficient in lateral mixing term
M_{b1} :Cross-shore flux of the longshore momentum due to mass transport under bores
M_{b2} :Cross-shore flux of the cross-shore momentum due to mass transport under bores
M_{b3} :Longshore flux of the longshore momentum due to mass transport under bores
M_w :Cross-shore flux of the longshore momentum in the surf zone
P_b :Fraction of breaking waves
$(P_b)_{bar}$:Fraction of breaking waves on a bar crest
S :Directional spectral density of a wave component
S_{xx}, S_{xy}, S_{yy} :Radiation stress components
$(s_{max})_{ob}$:Spreading parameter at the offshore boundary
T :Wave period
T_0 :Significant wave period at the water depth of 23.4m
$(T_{1/3})_{ob}$:Significant wave period at the offshore boundary
t :Time
$\tan\beta$:Beach slope
$\tan\beta_{bar}$:Beach slope in the offshore side of a bar crest
U :Depth and time-averaged longshore velocity
U_{EMC} :Longshore current velocity measured with the current meter
U_{FLOAT} :Longshore current velocity measured with the float
U_{ave} :Averaged velocity of longshore current between the tip of the HORF and a tough
U_{peak} :Peak velocity of longshore current between the tip of the HORF and a tough
V :Depth and time-averaged cross-shore velocity
V_1 :Depth and time-averaged velocity between wave trough and bottom
V_r :Velocity of return flow in a steady two-dimensional situation
$V_u(z)$:Time-averaged velocity in the wave direction at the elevation of z over the wave trough
$v_m(z)$:Maximum orbital velocity at the elevation of z
x :Longshore distance
y :Offshore distance
y_{bar} :Offshore distance of a bar crest
y_{peak} :Offshore distance of the location of a peak longshore velocity over a bar and a trough
y_{trough} :Offshore distance of a trough
z :Elevation relative to the datum level in Hasaki
Γ :Dimensionless coefficient in the wave transformation model
γ :Wave height-water depth ration constant in the surf zone
δ f :Frequency band width
$\delta\theta$:Directional band width
ϵ :Lateral mixing coefficient
η :Elevation of water surface

$\overline{\eta}$:Elevation of mean water level
θ :Wave direction
θ_p :Principal wave direction
$(\theta_p)_{ob}$:Principal wave direction at the offshore boundary
$(\theta)_{tip}$:Incident wave angle visually observed at the tip of the HORF
ρ :Density of sea water
σ :Angular frequency